PCCP

Highly efficient hydrogen production and selective CO_2 reduction by C_3N_5 photocatalyst using only visible light

Journal:	*Physical Chemistry Chemical Physics*
Manuscript ID	CP-ART-09-2023-004431.R1
Article Type:	Paper
Date Submitted by the Author:	21-Nov-2023
Complete List of Authors:	Ito, Kosei; Keio University Faculty of Science and Technology Graduate School of Science and Technology, Noda, Kei; Keio University Faculty of Science and Technology Graduate School of Science and Technology, Electronics and Electrical Engineering

ARTICLE

Highly efficient hydrogen production and selective CO_2 reduction by C_3N_5 photocatalyst using only visible light

Kosei Ito[a] and Kei Noda*[a]

Received 00th January 20xx,
Accepted 00th January 20xx

DOI: 10.1039/x0xx00000x

The production of energy sources by metal-free photocatalysts based on graphitic carbon nitride (g-C_3N_4) has garnered substantial attention. In this study, nitrogen-rich carbon nitride (C_3N_5) was successfully synthesized through the thermal polycondensation of 3-amino-1,2,4-triazole. The structural and physical characterization has suggested that a portion of the triazine rings, which constitute the structural framework of g-C_3N_4, may be substituted with five-membered rings in C_3N_5. Furthermore, the polymerization of C_3N_5 proceeded more extensively than that of g-C_3N_4 from melamine precursors. The increased nitrogen content in C_3N_5 resulted in a heightened number of π-electrons and a narrowed energy bandgap, with the potential of the valence band maximum being negatively shifted. Additionally, photocatalytic assessments encompassing nitro blue tetrazolium reduction, H_2 production from triethanolamine aqueous solution, and CO_2 reduction in the liquid phase were performed. All findings demonstrated that C_3N_5 exhibits significantly superior photocatalytic properties compared to g-C_3N_4. Particularly it is noteworthy that C_3N_5 selectively generates methanol and H_2 from oversaturated CO_2 solutions under visible light irradiation, while g-C_3N_4 selectively generates formaldehyde. These outcomes strongly indicate that C_3N_5 serves as a metal-free, visible-light-responsive photocatalyst, capable of contributing to both the production of renewable energy sources and the reduction of greenhouse effect gases.

Introduction

Since the first report of photocatalytic hydrogen generation using graphitic carbon nitride (g-C_3N_4) in 2009, g-C_3N_4 has attracted attention as an inexpensively, semi-permanently and easily synthesized metal-free photocatalytic material.[1-3] Prior research endeavors have reported more efficient H_2 production and CO_2 reduction by such as converting g-C_3N_4 from a two-dimensional material to a three-dimensional one and loading noble metal co-catalysts on it.[4,5] At present, the reaction efficiency of g-C_3N_4 is still notably inferior to that of metal compound photocatalysts. As long as continuing g-C_3N_4 studies just follow conventional approaches and methodologies that have been applied for metal compound photocatalysts with overwhelmingly high performance, it seems quite difficult to make carbon nitride materials exceed metal compound photocatalysts. However, if carbon nitride can exhibit photocatalytic properties comparable to those of metal compound photocatalysts, it would be an economically-viable choice and highly valuable for use from the viewpoints of sustainability and resource saving. Therefore, a fundamental structural reformulation of g-C_3N_4 is first required to create a metal-free photocatalyst that has capabilities like metal photocatalysts.

In the latest study, a new type of nitrogen-rich carbon nitride (C_3N_5) has been considered as an emerging photocatalytic material, because of its attractive features such as the smaller BG (ca. 2.1 eV) than that of g-C_3N_4, easier adsorption of organic compounds, faster charge transfer to metal cocatalysts, robustness against secondary contamination[6-9]. Furthermore, C_3N_5 was combined with other metal photocatalytic materials, which resulted in efficient H_2 production, CO_2 reduction, and organic decomposition.[10-12]

On the other hand, the reported C_3N_5 studies used metal-containing materials such as KBr during the synthesis process, and its photocatalytic properties are also evaluated in combination with other metal photocatalysts. This cancels out the attracting features of carbon nitrides that are easy-to-synthesize and metal-free. To effectively utilize the functions of carbon nitride, it is important to evaluate and compare inherent natures of existing materials (g-C_3N_4) and new ones (C_3N_5) and find important directions for materials development, rather than focusing on immediate property improvements. To date, we have not been able to find any papers that experimentally prove that C_3N_5 alone has better photocatalytic properties than g-C_3N_4 alone.

In this study, first, C_3N_5 was synthesized by only thermal polymerization from a precursor, without the use of metal-containing materials. Next, the detailed crystal structure and energy bands were evaluated. Finally, the photocatalytic properties of C_3N_5 were evaluated by H_2 production and CO_2 reduction, which were theoretically indicated as possible photocatalytic reactions in visible light over C_3N_5 owing to its conduction band (CB) and valence band (VB) edge positions.

---

[a] *Department of Electronics and Electrical Engineering, Keio University, 3-14-1, Hiyoshi, Kohoku-ku, Yokohama, 223-8522 Japan*
E-mail: nodakei@elec.keio.ac.jp

† Electronic Supplementary Information (ESI) available: See DOI: https://doi.org/10.1039/x0xx00000x

Similar experiments were also performed for g-C_3N_4 and the results for both C_3N_5 and g-C_3N_4 were compared and discussed. These experimental studies show that C_3N_5 is a better material than g-C_3N_4 for solving environmental and energy issues such as H_2 and CO_2 reduction, and provide new guidelines for the photocatalyst material design based on carbon nitride.

Experimental Methods

Materials and reagents

In this work, the following chemicals and reagents were purchased and used without any further purification: 3-amino-1,2,4-triazole (AT, $C_2H_4N_4$, Tokyo Chemical Industry), melamine monomer ($C_3H_6N_6$, Tokyo Chemical Industry), triethanolamine (TEOA, $N(CH_2CH_2OH)_3$, Nacalai Tesque; >98%), nitro blue tetrazolium (NBT) chloride ($C_{40}H_{30}Cl_2N_{10}O_6$, Tokyo Chemical Industry), terephthalic acid ($C_6H_4(COOH)_2$, Nacalai Tesque), and sodium hydroxide solution (NaOH, Nacalai Tesque; 5 M).

Synthesis of g-C_3N_4 and C_3N_5

C_3N_5 was synthesized by the following method. First, AT (3 g) was dissolved in 30 ml of pure water and stirred for 30 min. After that, the pure water was evaporated using an oil bath at 100 °C for 3 h and the remaining powder was dried under vacuum at 70 °C overnight. Finally, it was heated at a rate of 5 °C/min, kept at 550 °C for 2.5 h, and cooled naturally to room temperature. g-C_3N_4 was synthesized by thermal polycondensation of melamine (3 g) at a heating rate of 5 °C/min and at a holding temperature of 550 °C for 2.5 h.

Characterization

Morphology of the samples was investigated with a transmission electron microscope (TEM, Tecnai G2,FEI). Specific surface area measurements were performed using a commercially available adsorption analyzer (ASAP2020, Micromeritics). The chemical state informations were obtained by an X-ray photoelectron spectroscopy instrument (XPS, JPS-9010TR, JEOL) with Al-Kα radiation and a Fourier transform infrared spectroscopy (FTIR) system (ALPHA, Bruker). The crystal structure was specified by an X-ray diffractometer (XRD, D8 ADVANCE, Bruker) with Cu-Kα radiation. To examine the detailed energy band structure, diffuse-reflectance ultraviolet-visible (UV-Vis) absorption spectra were monitored by a UV-visible-near-infrared (UV-Vis-NIR) spectrophotometer (UV-3600Plus, Shimadzu) with an integration sphere. In addition, the determination of the flat band (FB) potential was performed by Mott-Schottky analysis with an electrochemical impedance analyzer (VersaSTAT3, AMETEK). For electrochemical impedance (EI) measurements, a 0.5 M Na_2SO_4 aqueous solution was employed as a liquid electrolyte, and an Ag/AgCl and a platinum wire were used as reference and counter electrode, respectively.

Photocatalytic hydrogen production using TEOA solution and photoreducing power assessment with NBT solution

45 ml of pure water, 5 ml of TEOA, and 300 mg of carbon nitrides were put into a 50 ml beaker and stirred for 30 min. After the beaker was placed inside a home-made measurement cell with gas circulation, the gas lines were purged with argon and gas was circulated in a closed system. Subsequently, visible light (λ > 385 nm) from a xenon lamp (MAX-303, Asahi Spectra) was irradiated onto the photocatalyst samples through the quartz window of the measurement cell, and the generated gas was analysed every 1 hour after the onset of the light irradiation, by a gas chromatograph (GC-8A, Shimadzu) equipped with a thermal conductivity detector (TCD) and packed columns (ShinCarbonST, Shinwa Kako).

30 ml of 5.0×10^{-5} M NBT aqueous solution and 10 mg of the synthesized carbon nitrides were added into a 50 ml beaker and stirred in the dark for 1 h. After visible light (λ > 385 nm) from a xenon lamp (MAX-303, Asahi Spectra) was irradiated for 5 min, 3 ml of the solution was centrifuged to separate the carbon nitride powder from the NBT solution. Then, the absorbance of NBT at 260 nm was measured with the UV-Vis-NIR spectrophotometer. NBT is oxidized to formazan by superoxide anions ($\cdot O_2^-$) formed by photocatalytic reduction of dissolved oxygen in solution.[13] NBT has a maximum absorption wavelength at around 260 nm, while the formazan reveals a maximum absorption at around 530 nm. [14] Since formazan is prone to be adsorbed on the catalyst surface and cannot be easily removed from the catalyst sample, the change in the absorbance of NBT was employed as an indicator of photoreducing power of the catalyst in this study.[15]

CO_2 photoreduction in liquid phase

50 ml of pure water and 300 mg of carbon nitrides were added into a 50 ml beaker and bubbled with pure CO_2 (99.9%) for 8 min. After that, a similar procedure as mentioned in the photocatalytic H_2 production measurement was employed to detect the products generated during CO_2 photoreduction. The solution in the beaker after the experiments was analysed by another gas chromatograph (GC2014, Shimadzu) with a TCD and packed columns (Sunpak-H, Shinwa Kako) using helium carrier gas. Gas analysis was also performed by the same gas chromatograph using packed columns (ShinCarbonST, Shinwa Kako) with argon carrier gas. The OH radicals formed on the photocatalyst surface were measured using the photoluminescence (PL) method. For this experiment, 10 mg of carbon nitrides, 0.04 g of terephthalic acid as a probe molecule, and 0.3 ml of NaOH which is a reagent dissolving the terephthalic acid and preventing quenching of the fluorescent material, were added to 30 ml of an oversaturated CO_2 solution. Subsequently, visible light (λ > 385 nm) was irradiated for 10 minutes, and only 3 ml of the solution was collected after centrifugation. When the OH radicals generated by the photocatalytic reaction interact with terephthalic acid, a highly fluorescent compound, 2-hydroxyterephthalic acid, is formed. The PL emission spectrum of this solution containing 2-hydroxyterephthalic acid was analysed using a fluorescence spectrophotometer (RF-6000, Shimadzu), with excitation and emission wavelengths set at 315 nm and 425 nm, respectively.

Results and discussion

Morphology and materials characterization

The TEM observations presented in Fig. 1 show that synthesized C_3N_5 and g-C_3N_4 have plate-like layer structures (Fig. 1a-b) and that C_3N_5 has a much larger plate size (ca. 5 μm) than g-C_3N_4 (ca. 1 μm) (Fig. 1c-d). This means that the polymerization in C_3N_5 proceeded more prominently than in g-C_3N_4. Brunauer-Emmett-Teller (BET) specific surface areas of the C_3N_5 and g-C_3N_4 samples were measured to be 2.6 and 5.4 m^2/g, respectively, which are well-correlated with the plate sizes estimated from Fig. 1.

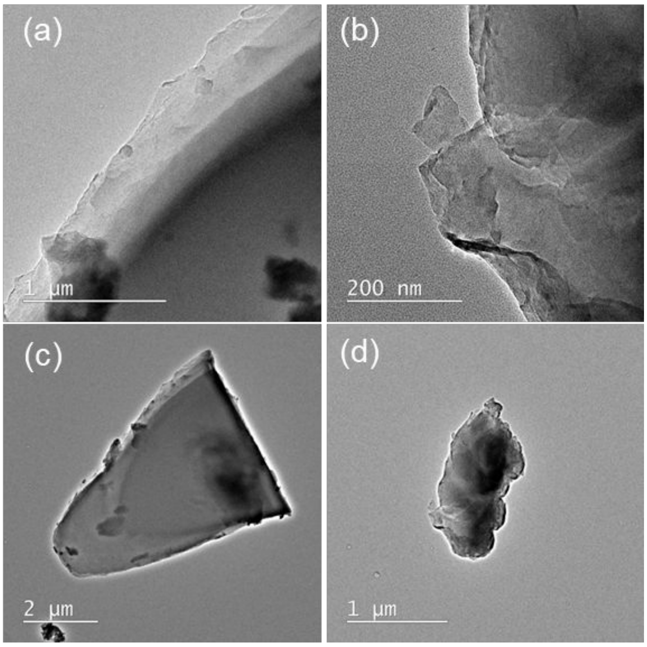

Fig. 1 TEM images of (a) C_3N_5 and (b) g-C_3N_4 particles. Low magnification TEM images of the same (c) C_3N_5 and (d) g-C_3N_4 particles are also presented.

In FTIR transmission spectra of the synthesized C_3N_5 and g-C_3N_4 (Fig. 2a), some characteristic absorption bands for carbon nitride species appeared. An absorption peak at 800-900 cm^{-1} originates from triazine rings, broad bands in the range from 1100 to 1700 cm^{-1} derive from C-N and C=N bonds, and the bands at 2900-3400 cm^{-1} are due to the end groups such as C-N-H, N-H, and O-H.[16.17] Although the broad absorption bands from 1100 to 1700 cm^{-1} did not show any significant difference between these two samples, the peak at 800-900 cm^{-1} in C_3N_5 was smaller than that in g-C_3N_4, presumably because a portion of the triazine rings was replaced with five-membered rings derived from the AT precursor in C_3N_5. Several literatures have reported that some of the precursor backbone exist in synthesized samples, and C_3N_5 precursor (AT) molecule owns a five-membered ring.[18-20] Also, the absorbance of the bands from 2900 to 3400 cm^{-1} in C_3N_5 seems somewhat smaller than that in g-C_3N_4. As we discussed with the TEM images (Fig. 1) and the BET specific surface areas, the C_3N_5 plate size was larger than that of g-C_3N_4, resulting in the smaller number of end groups in C_3N_5 sheets.

The compositional ratio of carbon and nitrogen atoms (C/N) in the synthesized C_3N_5 and g-C_3N_4 was calculated from XPS spectra (Fig. 2b-c), where the N1s and C1s signals were deconvoluted by using a Gaussian-Lorentzian function. The C/N ratio was given as the ratio between the peak area of C1s signal divided by the sensitivity of 4.079 and that of N1s signal divided by the sensitivity of 7.041. As a result, the calculated C/N ratio was 3 : 4.93 for C_3N_5 and 3 : 3.96 for g-C_3N_4, respectively, supporting that the chemical composition is almost stoichiometric for both C_3N_5 and g-C_3N_4.

In the narrow-scan N1s spectra (Fig. 2b), the C-N-C peaks are assigned to be triazine frameworks, the N-$(C)_3$ peaks are heptazine ring nucleus and the bridges between the heptazine rings, and the N-H and N-OH are end groups. [21-23] The ratios among respective signals (C-N-C : N-$(C)_3$: N-H and N-OH) were 14 : 67 : 19 for C_3N_5 and 28 : 50 : 22 for g-C_3N_4, respectively. The larger ratio of N-$(C)_3$ and the smaller ratio of N-H and N-OH for C_3N_5 indicate the grain size enlargement, which was in line with the TEM observation results (Fig. 1) and measured specific surface areas. Additionally, the relative intensity of C-N-C in C_3N_5 was smaller than that in g-C_3N_4, which probably reflects the partial replacement of six-membered rings in the triazine frameworks with five-membered rings, as we discussed in the FTIR spectra (Fig. 2a). Furthermore, a small π-electron peak was observed at around 404 eV in only C_3N_5, where n-π* transition can be promoted by the increase in the number of unshared electron pairs with an increasing nitrogen content.[24] Besides, the main peak position of N1s binding energy in C_3N_5 (398.2 eV) is shifted negatively from that of g-C_3N_4 (398.7 eV). Since C_3N_5 has more π electrons, the electron density in C_3N_5 becomes larger than that in g-C_3N_4. As a result, the binding energy is considered to become shifted negatively.[25.26] As presented in Fig. S1 (ESI†), the peak area of O1s signal in C_3N_5 (4.55×10^4) is smaller than that of g-C_3N_4 (5.70×10^4). Since the oxygen peaks are derived from adsorbed oxygen species and end OH groups,[27.28] this decrease in the O1s peak intensity of C_3N_5 correlates with the larger C_3N_5 particle size.

Based on these FTIR and XPS data, the structures of C_3N_5 and g-C_3N_4 are schematically drawn in Fig. 2d.

XRD profiles in Fig. 2e reveal that both samples displayed 100 and 002 reflections. The 100 peak indicates in-plane ordering of the two-dimensional direction, and the 002 peak indicates interphase stacking of the carbon nitride sheets.[29.30] The 002 peak position of C_3N_5 (27.68°) was shifted to higher diffraction angle than that of g-C_3N_4 (27.43°). Considering that C_3N_5 has more π-electrons, the C_3N_5 layers are attracted to each other by π-π interactions more strongly than the g-C_3N_4 layers. Therefore, the 002 peak of C_3N_5 was shifted to a higher diffraction angle.

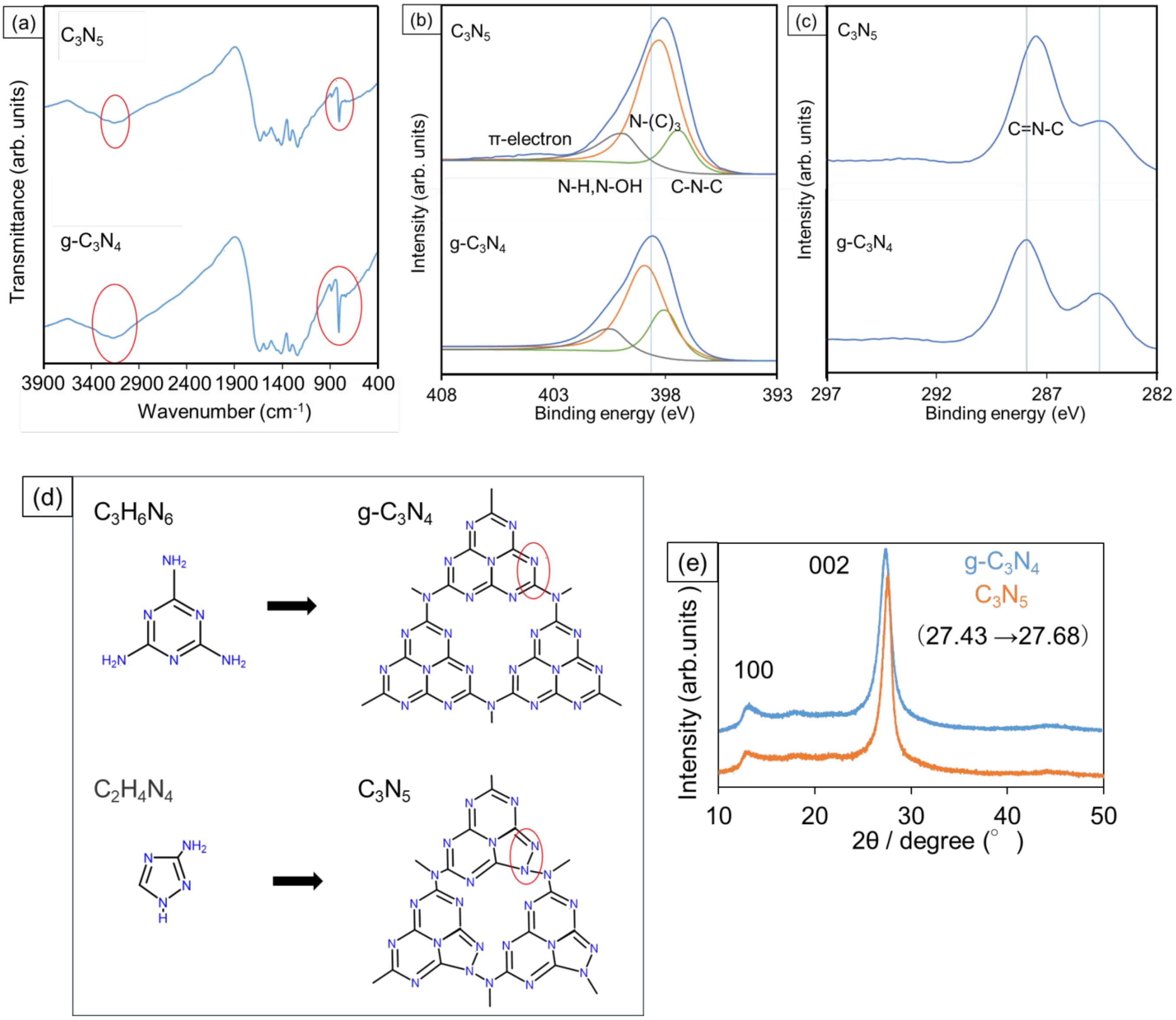

Fig. 2 (a) FTIR spectra and XPS spectra of (b) N1s and (c) C1s signals measured for C_3N_5 and g-C_3N_4 samples. (Peaks at 284.6 eV were used for charge correction.) (d) Structural diagrams of polymerization for C_3N_5 and g-C_3N_4. (e) XRD patterns for C_3N_5 and g-C_3N_4.

Energy band structure

Tauc plot analysis was carried out for estimating band gap (BG) energy of the samples. Fig. 3a presents the Tauc plots obtained from the measured diffuse-reflectance UV-Vis absorption spectra under the assumption that C_3N_5 and g-C_3N_4 have indirect bandgaps.[31,32] In Fig. 3a, α is the light absorbance, h the Planck constant, and ν the light frequency, respectively. The estimated BG values of C_3N_5 and g-C_3N_4 are 2.15 and 2.75 eV.

Mott-Schottky (M-S) analysis was performed to further investigate energy band structure. The carbon nitrides were deposited onto fluorine-doped tin oxide (FTO) substrates in the same way as for the powder synthesis, except that an FTO substrate was placed on top of the powder sample during the high-temperature treatment. The applied potential (V) and measured space charge capacitance (C) at various modulation frequencies produced M-S plots ($1/C^2$-V curves) as shown in Fig. 3b-c. The positive slopes in the obtained M-S plots indicate that the synthesized C_3N_5 and g-C_3N_4 are n-type semiconductors.[33,34] If we assume that the conduction band (CB) edge is about 0.2 V more negative than the FB level of n-type semiconductor, the CB edge positions of C_3N_5 and g-C_3N_4 films were calculated to be −0.77 V (vs normal hydrogen electrode(NHE)) and −0.78 V (vs NHE), respectively.[35,36] The valence band (VB) edge positions of C_3N_5 and g-C_3N_4 were also determined to be 1.38 V (vs NHE) and 1.97 V (vs NHE), respectively, by taking their BG energy values into account. XPS valence band spectra (Fig. 3d-e) revealed that the VB edge of C_3N_5 was more negative than that of g-C_3N_4, which was consistent with the above-described results. The energy band diagrams of the synthesized C_3N_5 and g-C_3N_4 are schematically depicted in Fig. 3f. The BG of carbon nitride

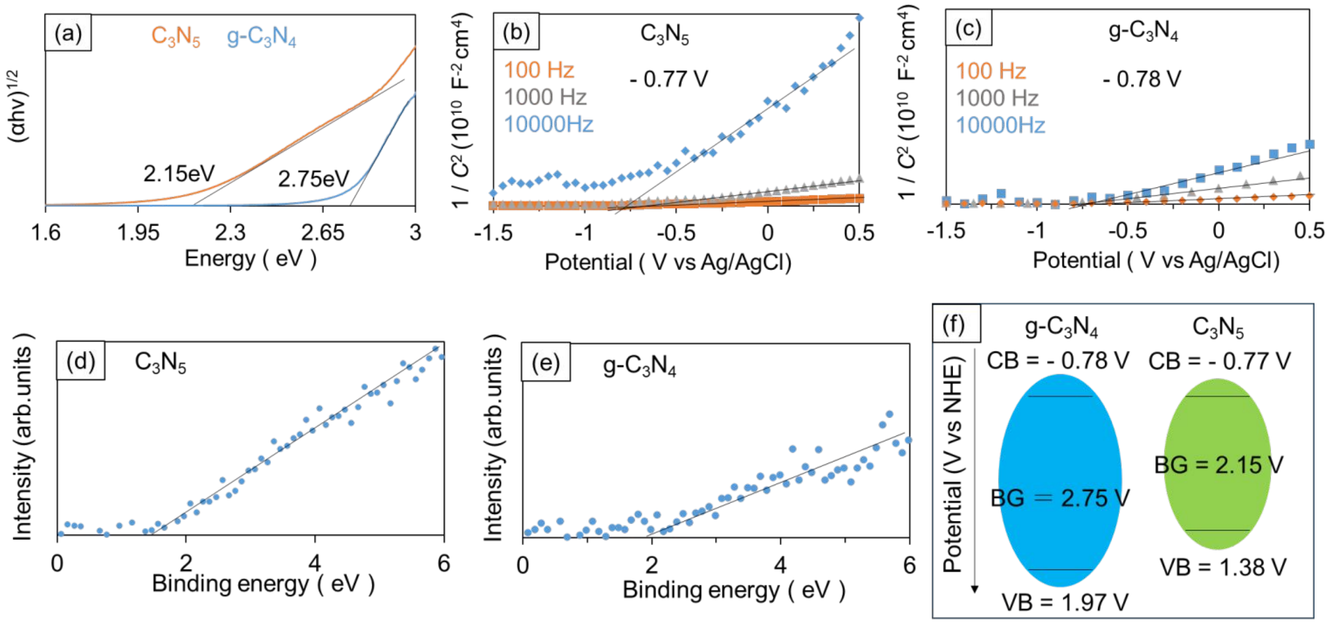

Fig. 3 (a) Tauc plots obtained from UV-Vis absorption spectra for C_3N_5 and g-C_3N_4 (The obtained BG values were given in the figure). Mott-Schottky plots measured for (b) C_3N_5 and (c) g-C_3N_4 (The obtained FB potentials were provided in the figures). XPS valence band spectra of (d) C_3N_5 and (e) g-C_3N_4. (f) Schematic drawing of energy band diagrams of C_3N_5 and g-C_3N_4.

materials is determined by the N2p orbital for VB and the C2p orbital for CB.[37.38] The narrower BG of C_3N_5 is attributed to the shallower VB level because C_3N_5 is richer in nitrogen than g-C_3N_4 and has more nitrogen-derived π electrons.

Photocatalytic hydrogen production over C_3N_5 and g-C_3N_4

Fig. 4 shows the photocatalytic H_2 production from TEOA solution over C_3N_5 and g-C_3N_4, respectively. The H_2 production rate of C_3N_5 (ca. 1.2 µmol h^{-1}) was almost twice as high as that of g-C_3N_4 (ca. 0.6 µmol h^{-1}). Photocatalysis always involves a similar number of holes used for oxidation reactions and electrons used for reduction reactions. Both C_3N_5 and g-C_3N_4 meet the oxidation potential (1.23 V (vs. NHE)) and reduction potential (0 V (vs. NHE)) for hydrogen production from water.[39.40] But when water contains sacrificial reagents, they are preferentially oxidized and this photooxidation reaction proceeds fast.[41] In this case, the rate-determining process must be a two-electron reduction of protons produced by the oxidation reaction. Therefore, the reason why C_3N_5 could generate hydrogen more efficiently than g-C_3N_4 can be ascribed to the improved reducing power of C_3N_5.

NBT measurements (Fig. 5) also suggested that C_3N_5 has better reducing power than g-C_3N_4. The reducing power of C_3N_5 is enhanced by the large reduction in BG by the negative shift of VB edge and by the increase in the number of excited electrons by visible light irradiation, despite the similar structures and almost identical CB edge positions between C_3N_5 and g-C_3N_4.

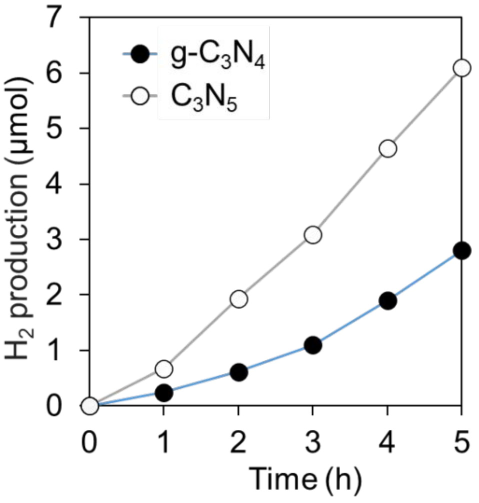

Fig. 4 Amount of H_2 production from TEOA aqueous solution over C_3N_5 and g-C_3N_4 under VIS irradiation.

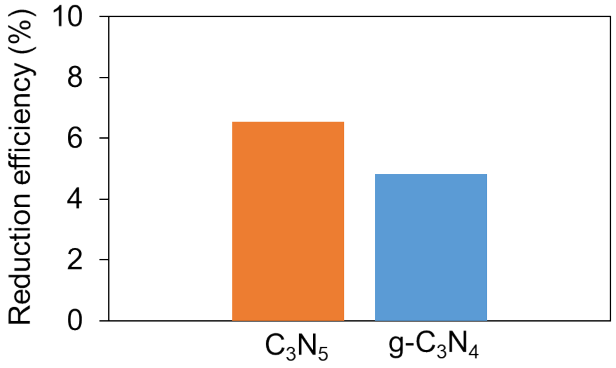

Fig. 5 Efficiency of NBT reduction caused by O_2 radicals produced over C_3N_5 and g-C_3N_4.

Liquid phase CO_2 photoreduction over C_3N_5 and g-C_3N_4

The experimental results of CO_2 photoreduction in water under oversaturated condition were provided in Fig. 6a-b. C_3N_5 selectively produced methanol (CH_3OH) and H_2, while g-C_3N_4 produced only formaldehyde (CH_2O). No other gases and liquids, except CO_2, were observed (Fig. 6c). In Fig. 6c, the pH of CO_2 aqueous solution was 3.9 immediately after preparing oversaturation condition and was gradually raised up to 5.6 after 2 h in the dark. In general, the pH of pure water is 6 to 6.5, and when CO_2 is dissolved, it tends to be more acidic depending on its concentration.[42.43] In other words, the detection of CO_2 gas and the change in pH verify that CO_2 was present in excess in the water.

As shown in Fig. 6, the time variation of the gas production (CH_3OH, CH_2O, H_2) amounts, pH of the solution, and the CO_2 amount become almost unchanged after 2 h passed from the start of the measurements. The reaction kinetics depends on temperature, activation energy, and concentration of gases.[44] In the present experiment, the temperature was constant during 3 h after the start of the measurements. On the contrary, the concentration of CO_2 dissolved in the solution decreased significantly over time. Hence, the chemical reaction rate of CO_2 reduction was relatively high at the initial stage of the photocatalytic experiment due to the presence of CO_2 in an oversaturated state, while the reaction rate became lowered with the rapid decrease in the CO_2 concentration in the solution.

In the case of simple CO_2 reduction, CO is usually detected as an intermediate.[45.46] However, CO was not detected in our measurements (Fig. 6). This indicates that CO_2 directly produces CH_3OH and CH_2O by multi-electron reduction.

$$CO_2 + 6H^+ + 6e^- \rightarrow CH_3OH + H_2O \qquad (1)$$

$$CO_2 + 4H^+ + 4e^- \rightarrow CH_2O + H_2O \qquad (2)$$

Six electrons are required for the generation of CH_3OH, and four electrons are required for the generation of CH_2O. Nevertheless, the quantity of CH_3OH produced by C_3N_5 (0.17 μmol) is greater than that of CH_2O produced by g-C_3N_4 (0.12 μmol) (Fig. 6a).

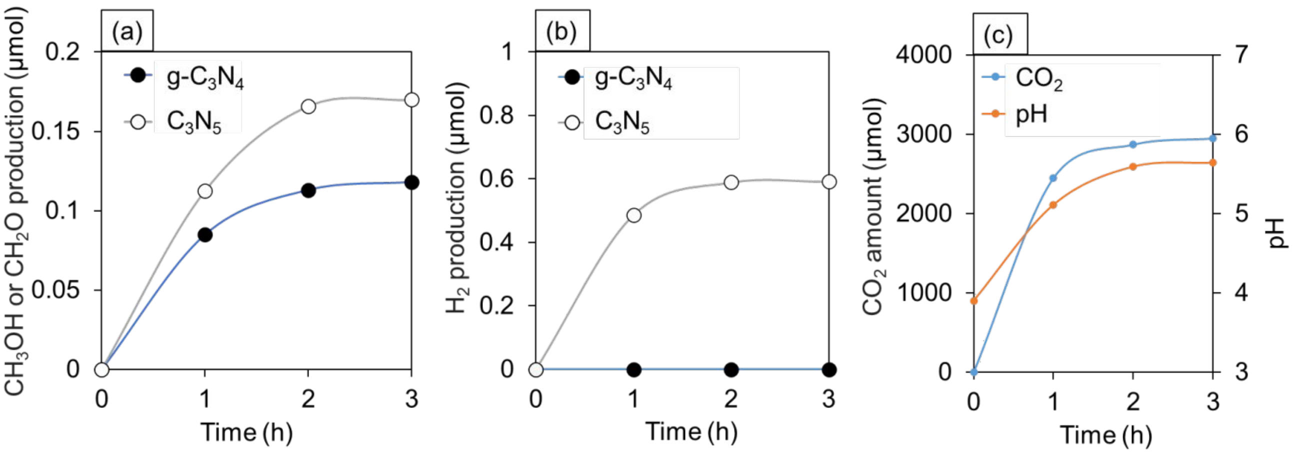

Fig. 6 Amounts of (a) CH_3OH or CH_2O and (b) H_2 production from oversaturated CO_2 aqueous solution over C_3N_5 and g-C_3N_4 under VIS irradiation. (c) Temporal changes in CO_2 amount detected by gas chromatograph and pH of the CO_2 aqueous solution with no catalyst under VIS irradiation.

Some possible reasons why these reactions could occur are provided as follows.

It has been reported that when the CO_2 concentration near the catalyst is high, the final substance is formed directly from CO_2.[47] Additionally, both g-C_3N_4 and C_3N_5 have narrow BGs, and they have larger number of excited electrons. These situations may have induced multi-electron reduction and allowed direct reduction to the final material.[48] C_3N_5 may have produced CH_3OH by six-electron reduction because of its narrower BG than g-C_3N_4. [49] It is also worth noting that no byproduct radical species were generated. In general, the generation of radical species could be one of the key factors that promote the formation of intermediates such as CO and CH_4 in the reduction of CO_2.[50] However, OH radicals were not produced under our experimental condition (Fig. S2, ESI†). This is because, VB edges of C_3N_5 and g-C_3N_4 are far from the redox potential to generate OH radicals [$E(H_2O/OH\cdot) = 2.72$ V (vs NHE)], and therefore, they would not be able to produce OH radicals from water.[51] In addition, under the conditions of the current experiment, O_2 radicals are not produced because dissolved oxygen is no longer present due to the CO_2 bubbling.

CO_2 dissolved in water is known to exist in the form of CO_2 (aq), carbonic acid (H_2CO_3), and carbonate ions (HCO_3^-).[52]

$$CO_2 + H_2O \rightleftarrows CO_2\,(aq) + H_2CO_3 \rightleftarrows H^+ + HCO_3^- \qquad (3)$$

It has been reported that the CO_2 concentration in CO_2 (aq) is approximately 500 times as large as that of H_2CO_3, and the concentration of H_2CO_3 in the solution is from 23 to 71 times greater than that of HCO_3^-.[53] Although the concentration of H_2CO_3 is quite low, the reaction pathway via H_2CO_3 formation should be regarded. Taking thermodynamics into consideration, as the reduction potential of the H_2CO_3/CH_3OH pair (0.044 V (vs NHE)) is more positive than that of CO_2/CH_3OH (−0.38 V (vs NHE)), H_2CO_3 reduction will be more favorable than CO_2 reduction.[54.55] The same is true for the CH_2O formation because the reduction potentials of H_2CO_3/CH_2O and CO_2/CH_2O are

−0.05 V (vs NHE) and −0.52 V (vs NHE), respectively.[55] The reaction pathways of H_2CO_3 reduction are not routed through carbon monoxide (CO) as an intermediate, which is consistent with our results without CO generation (Fig. 6).[53.55] From Fig. 3f, the CB edges of both C_3N_5 and g-C_3N_4 meet the reduction potentials to produce CH_3OH and CH_2O from H_2CO_3. Accordingly, CO_2 reduction via H_2CO_3 formation is one of the plausible scenarios in this work.

The oxidation reaction route can generate protons from pure water, that are essential for the formation of CH_3OH and CH_2O.

$$2H_2O + 4h^+ \rightarrow 4H^+ + O_2 \qquad (4)$$

Here, we would like to note that protons can be slightly produced by reversible reaction of CO_2 in water (eqn (3)). Also, no change in the amount of CH_3OH and H_2 produced after 2 and 3 h (Fig. 6a-b) reflects that the oversaturated CO_2 solution is the source of H_2, and that CH_3OH does not contribute to the production of H_2.

Additional control experiments (Fig. S3, ESI†) clearly show that this photocatalytic CO_2 reduction was caused by C_3N_5 and g-C_3N_4. As for photocatalytic cycle test, CO_2 reduction experiment over C_3N_5 was performed three times, which resulted in no change in photocatalytic activity (Fig. S4, ESI†). Furthermore, XRD and TEM observations of the samples after the photocatalytic measurements revealed no significant changes in the morphology and crystal structure of C_3N_5 (Fig. S5 and Fig. S6, ESI†). The above results indicate that C_3N_5 is chemically stable while g-C_3N_4 is reported to be chemically unstable. The increased number of π-electrons may allow orbital interactions and improve the chemical stability of C_3N_5.[56]

Conclusions

We have successfully synthesized C_3N_5, a nitrogen-abundant carbon nitride, by thermal polycondensation using 3-amino-1,2,4-triazole as a precursor. TEM images and specific surface area measurements showed that the synthesized C_3N_5 has a larger grain size than g-C_3N_4 prepared from melamine precursors, and that polymerization proceeds more easily in C_3N_5. XPS and FTIR studies suggested that part of the triazine frameworks in nitrogen-rich C_3N_5 is comprised by five-membered rings. Then, the increase in nitrogen atoms with unshared electron pairs leads to the generation of more π-electrons in C_3N_5. This increase is reflected in the shorter interlayer distance of C_3N_5 with stronger π-π interactions. Furthermore, experimentally obtained energy band alignments revealed that C_3N_5 has a narrower band gap than g-C_3N_4 owing to a large negative shift of the valence band maximum dominated by N2p orbitals, which may also be attributed to the increased π-electrons in C_3N_5.

In the photocatalytic H_2 production from TEOA solution, the rate of H_2 production for C_3N_5 was about twice as high as that for g-C_3N_4. Considering the results of the NBT experiment, the promotion of the rate-determining proton reduction might lead to more efficient hydrogen production. Finally, in the liquid phase CO_2 photoreduction, C_3N_5 selectively produced CH_3OH and H_2, while g-C_3N_4 selectively produced CH_2O. The amount of CH_3OH produced by C_3N_5 was greater than that of formaldehyde produced by g-C_3N_4, indicating that C_3N_5 is more capable of multi-electron reduction than g-C_3N_4. To understand the observed product selectivity in the CO_2 photoreduction, two possible reaction pathways were considered and discussed based on the reversible changes of CO_2 in the water.

Eventually, all photocatalytic experiments in this study supported our idea that C_3N_5 alone has better photocatalytic properties than g-C_3N_4 alone. The results of this research will guide the synthesis of novel metal-free photocatalysts and contribute, in part, to triggering new breakthroughs for their practical applications.

Author Contributions

Conceptualization: K. I. and K. N., Methodology: K. I. and K. N., Investigation: K. I., Data Curation: K. I., Supervision: K. N., Project administration: K. N., Writing-original draft: K. I. and K. N., Writing-review & editing: K. I. and K. N.

Conflicts of interest

There are no conflicts to declare.

Acknowledgements

This work was supported by a Grant-in-Aid for Scientific Research (KAKENHI No. 19H02174) of the Japan Society for the Promotion of Science (JSPS). K. I. is very grateful to the supports from JST SPRING Grant Number JPMJSP2123.

Notes and references

1 X. Wang, K. Maeda, A. Thomas, K. Takanabe, G. Xin, J. M. Carlsson, K. Domen, M. Antonietti, Nat. Mater., 2009, 8, 76-80.

2 P. Chen, X. Dong, M. Huang, K. Li, L. Xiao, J. Sheng, S. Chen, Y. Zhou, F. Dong, ACS Catal., 2022, 12, 4560-4570.

3 N. Jiang, L. Lyu, G. Yu, L. Zhanga, C. Hu, J. Mater. Chem. A, 2018, 6, 17819-17828.

4 X. Wang, J. Gong, Y. Dong, S. An, X. Zhang, J. Tian, Mater. Today Phys., 2022, 27, 100806.

5 S. Tasleem, M. Tahir, Int. J. Hydrog. Energy, 2021, 46, 20995-21012.

6 P. Kumar, E. Vahidzadeh, U. K. Thakur, P. Kar, K. M. Alam, A. Goswami, N. Mahdi, K. Cui, G. M. Bernard, V. K. Michaelis, K. Shankar, J. Am. Chem. Soc., 2019, 141, 5415-5436.

7 J. Zhang, B. Jing, Z. Tang, Z. Ao, D. Xia, M. Zhu, S. Wang, Appl. Catal. B, 2021, 13, 24907-24915.

8 H. Che, J. Wang, X. Gao, J. Chen, P. Wang, B. Liu, Y. Ao, J. Colloid Interface Sci., 2022, 627, 739-748.

9 J. Liu, S. Wang, C. Zhao, J. Zheng, Nanomaterials, 2023, 13, 499.

10 L. Wang, R. Chen, Z. Zhang, X. Chen, J. Ding, J. Zhang, H. Wan, G. Guan, J. Environ. Chem. Eng., 2023, 11, 109345.

11 S, Vadivel, M. Fujii, S. Rajendran, Chemosphere, 2022, 307, 135716.

12 S. Li, M. Cai, Y. Liu, J. Zhang, C. Wang, S. Zang, Y. Li, P. Zhang, X. Li, Inorg. Chem. Front., 2022, 9, 2479-2497.
13 W. Yang, K. Sun, J. Wan, Y-A. Ma, J. Liu, B. Zhu, L. Liu, F. Fu, Appl. Catal. B, 2023, 320, 121978.
14 C. Zhua, Y. Zhanga, Z. Fana, F. Liua, A. Li, J. Hazard. Mater., 2020, 393, 122395.
15 C-H Chang, C-L Wang, B-R Li, Biosens. Bioelectron., 2023, 236, 115403.
16 J. Xu, L. Zhang, R. Shi, Y. Zhu, J. Mater. Chem. A, 2013, 1, 14766-14772.
17 Z. Xiong, Y. Liang, J. Yang, G. Yang, J. Jia, K. Sa, X. Zhang, Z. Zeng, Sep. Purif. Technol., 2023, 306, 122522.
18 A. Krishnan, M. Yoosuf, K. Archana, A.S. Arsha, A. Viswam, J. Energy Chem., 2023, 80, 562-583.
19 W. J. Ong, L. L. Tan, Y. H. Ng, S. T. Yong, S.P. Chai, Chem. Rev., 2016, 116, 7159-7329.
20 Y. Zhao, J. Zhang, L. Qu, ChemNanoMat, 2015, 1, 298-318.
21 X. Wu, R. Zhong, X. Lv, Z. Hu, D. Xia, C. Li, B. Song, S. Liu, Appl. Catal. B, 2023, 330, 122666.
22 J. Ding, Q. Tang, Y. Fu, Y. Zhang, J. Hu, T. Li, Q. Zhong, M. Fan, H. H. Kung, J. Am. Chem. Soc., 2022, 144, 9576-9585.
23 X. Guan, M. Fawaz, R. Sarkar, C-H. Lin, Z. Li, Z. Lei, P. D. Nithinraj, P. Kumar, X. Zhang, J-H. Yang, L. Hu, T. Wu, S. Chakraborty, J. Yi, A. Vinu, J. Mater. Chem. A, 2023, 11, 12837-12845.
24 X. Li, D. Shen, C. Liu, J. Li, Y. Zhou, X. Song, P. Huo, H. Wang, Y. Yan, J. Colloid Interface Sci., 2019, 554, 468-478.
25 L. Yang, X. Liu, Z. Liu, C. Wang, G. Liu, Q. Li, X. Feng, Ceramics International, 2018, 44, 20613-20619.
26 L. V. Goncharova, Basic Surfaces and their Analysis, Morgan & Claypool Publishers, USA, 2018, 6, 1-17.
27 Q. Zhang, Z. Zhang, S. Xu, A. Liu, L. Da, D. Lin, C. Jiang, Anal. Chem., 2023, 95, 4536-4542.
28 X. Huang, X. Xu, R. Yang, X. Fu, Colloids Surf. A Physicochem. Eng. Asp., 2022, 643, 128738.
29 X. An, Q. Tang, H. Lan, H. Liu, X. Yu, J. Qu, H. Lin, J. Ye, Angew. Chem. Int. Ed., 2022, 134, e202212706.
30 B. Yang, J. Han, Q. Zhang, G. Liao, W. Cheng, G. Ge, J. Liu, X. Yang, R. Wang, X. Jia, Carbon, 2023, 202, 348-357.
31 P. V. Viet, T-D. Nguyen, D-P. Bui, C. M. Thi, J. Materiomics, 2022, 8, 1-8.
32 M. Mohammadikish, N. Mosleh, Appl. Organomet. Chem., 2023, e7177.
33 Z. Cai, Y. Huang, H. Ji, W. Liu, J. Fu, X. Sun, Sep. Purif. Technol., 2022, 280, 119772.
34 R. Ren, G. Liu, J. Y. Kim, R. E. A. Ardhi, M. X. Tran, W. Yang, J. K. Lee, Appl. Catal. B, 2022, 306, 121096.
35 X. Ma, Z. Ma, H. Zhang, D. Lu, J. Duan, B. Hou, J. Photochem. Photobiol. A, 2022, 426, 113772.
36 Y. Liang, X. Wu, X. Liu, C. Li, S. Liu, Appl. Catal. B, 2022, 304, 120978.
37 W. Hoa, Z. Zhanga, M. Xub, X. Zhang, X. Wang, Y. Huang Appl. Catal. B, 2015, 179, 106-112.
38 J. Chen, Y. Xiao, N. Wang, X. Kang, D. Wang, C. Wang, J. Liu, Y. Jiang, H. Fu, Sci. China Mater., https://doi.org/10.1007/s40843-023-2443-0.
39 D. Dai, X. Liang, B. Zhang, Y. Wang, Q. Wu, X. Bao, Z. Wang, Z. Zheng, H. Cheng, Y. Dai, B. Huang, P. Wang, Adv. Sci., 2022, 9, 2105299.
40 Y-J. Yuan, N. Lu, L. Bao, R. Tang, F-G. Zhang, J. Guan, H-D. Wang, Q-Y. Liu, Q. Cheng, Z-T. Yu, Z. Zou, ACS nano, 2022, 16, 12174-12184.
41 V. Kumaravel, M. D. Imam, A. Badreldin, R. K. Chava, J. Y. Do, M. Kang, A. A. Wahab, Catalysts, 2019, 9, 276.
42 H. Jun, S. Choi, M. Y. Yang, Y. S. Nam, J. Mater. Chem. A, 2019, 7, 17254-17260.
43 J. Byun, W. Huang, D. Wang, R. Li, K. A. I. Zhang, Angew. Chem. Int. Ed., 2018, 57, 2967-2971.
44 B. Liu, X. Zhao, C. Terashima, A. Fujishima, K. Nakata, Phys. Chem. Chem. Phys., 2014, 16, 8751-8760.
45 N. F. Khusnun, A. A. Jalil, T. A. T. Abdullah, S. S. M. Latip, C. N. C. Hitam, A. A. Fauzi, N. S. Hassan, M. A. H. Aziz, A. F. A. Rahman, F. F. A. Aziz, M. Bahari, R. H. Adnan, R. Saravanan, J. CO2 Util., 2022, 58, 101908.
46 X. Wanga, Y. Wanga, M. Gaob, J. Shenb, X. Puc, Z. Zhangb, H. Linb, X. Wang, Appl. Catal. B, 2020, 270, 118876.
47 A. B. Anderson, H. A. Asiri, Phys. Chem. Chem. Phys., 2014, 16, 10587-10599.
48 X. Wu, Y. Li, G. Zhang, H. Chen, J. Li, K. Wang, Y. Pan, Y. Zhao, Y. Sun, Y. Xie, J. Am. Chem. Soc., 2019, 141, 5267-5274.
49 A. Li, T. Wang, C. Li, Z. Huang, Z. Luo, J. Gong, Angew. Chem. Int. Ed., 2019, 58, 3804-3808.
50 M. Ma, Z. Huang, R. Wang, R. Zhang, T. Yang, Z. Rao, W. Fa, F. Zhang, Y. Cao, S. Yu, Y. Zhou, Green Chem., 2022, 24, 8791-8799.
51 K. Ito, R. Uchida, K. Noda, J. Photochem. Photobiol. A, 2023, 443, 114824.
52 T. Zhao, J. Li, J. Liu, F. Liu, K. Xu, M. Yu, W. Xu, F. Cheng, ACS Catal., 2023, 13, 4444-4453.
53 S. Pocoví-Martínez, I. Zumeta-Dube, D. Diaz, J. Nanomater., 2019, 6461493.
54 A. L. Soli, R. H. Byrne, Mar. Chem., 2002, 78, 65–73.
55 X. Yang, T. Xiao, P. P. Edwards, Int. J. Hydrog. Energy, 2011, 36, 6546-6552.
56 S. Shen, Y. Zeng, X. Li, L. Meng, X. Zhang, Int J Quantum Chem, 2018, 118, e25521.